Synthesis of Bi_2O_3/g-C_3N_4 for enhanced photocatalytic CO_2 reduction with a Z-scheme mechanism†

Hao Peng,[a] Rui-Tang Guo, [ID] *[bcd] He Lin*[a] and Xing-Yu Liu[bc]

Bi_2O_3/g-C_3N_4 nanoscale composites with a Z-scheme mechanism were successfully synthesized by high temperature calcination combined with a hydrothermal method. These synthesized composites exhibited excellent photocatalytic performance, especially the 40 wt% Bi_2O_3/g-C_3N_4 composite, which produced about 1.8 times the CO yield of pure g-C_3N_4. The obtained products were characterized by X-ray diffraction (XRD) patterns, X-ray photoelectron spectroscopy (XPS), scanning electron microscope (SEM), transmission electron microscopy (TEM), Brunauer–Emmett–Teller (BET), UV-vis diffuse reflectance spectroscopy (UV-vis DRS) and so on. Characterization results revealed that Bi ions had well covered the surface of g-C_3N_4, thus restraining the recombination of electron–hole pairs and resulting in a stronger visible-light response and higher CO yield. In addition, the electron transfer process through the Z-scheme mechanism also promoted the photocatalytic activity.

1. Introduction

In recent years, the continuous development of industry and the serious destruction of forest vegetation have led to difficulties in controlling CO_2 emission, thus seriously threatening the survival and development of mankind.[1–6] Recently, the field of CO_2 photocatalytic reduction which translates CO_2 into some useful substances has attracted many research teams.[7–12] As we all know, many narrow band gap semiconductor based photo-catalysts have been used in CO_2 photocatalytic reduction.[13–15] Among them, g-C_3N_4 is the most widely used one due to its suitable band gap, simple and convenient preparation and good visible light response.[16,17] However, there are still many obvious shortcomings associated with this catalyst, such as its small range of light response, low separation rate of electron–hole pairs and unsatisfactory performance in the photocatalytic reaction. Lots of methods have been developed to improve the photocatalytic performance of g-C_3N_4, such as element modification,[18–20] texture fabrication[21,22] and heterojunction formation.[23–27] Fabrication of a heterojunction between two semiconductors is a promising way among these methods, in which the formation of an internal electric field and the promoted separation of charge carriers effectively restrains the recombination rate of electron–hole pairs.[28]

As an important semiconductor material, Bi_2O_3 has been applied in many fields like electronic ceramics, optoelectronic devices, high-temperature superconductors, catalysts, and sensors due to its special physical properties and crystal structure.[29–33] What's more, Bi_2O_3 also has been used as a normal photocatalyst in water splitting and photodegradation pollutant. Unfortunately, its photoreduction performance is poor owing to the low migration of photo-charges, which leads to a fast combination of photogenerated electron–hole pairs.[34–37] For the improvement of photocatalytic ability over Bi_2O_3, the construction of heterojunction is considered as an effective measure to reduce the probability of electron–hole pairs recombination, like BiOCl/Bi_2O_3,[38] $BiVO_4$/Bi_2O_3 (ref. 39) and Bi_2O_3/TiO_2.[40] It is known that an internal electric field is produced after the formation of a p–n heterojunction. The photocarriers are greatly accelerated by the electric field, which effectively suppresses the reflux of photogenerated carriers and thus improves the photocatalytic performance.[41] Due to the presence of heterojunctions, the excitation wavelength of light is also extended at the same time.[42]

From the above analysis, it can be presumed that there exists a possibility to construct a heterostructure between Bi_2O_3 and g-C_3N_4 through their mutual activation. However, the use of Bi_2O_3/g-C_3N_4 heterojunctions for CO_2 photoreduction has not been reported. Therefore, Bi_2O_3/g-C_3N_4 compounds with different Bi_2O_3 contents were prepared and used in CO_2 photocatalytic reduction in this study. It was found that the yields of Bi_2O_3/g-C_3N_4 compounds was higher than single Bi_2O_3 or g-

[a]School of Mechanical and Power Engineering, Shanghai Jiaotong University, Shanghai 200240, China. E-mail: linhe@sjtu.edu.cn

[b]College of Energy and Mechanical Engineering, Shanghai University of Electric Power, Shanghai, China. E-mail: grta@zju.edu.cn

[c]Shanghai Engineering Research Center of Power Generation Environment Protection, Shanghai, P. R. China

[d]Shanghai Institute of Pollution Control and Ecological Security, Shanghai, 200092, P. R. China

C_3N_4. Moreover, the visible light response is also enhanced. Based on the results of all the characterization techniques, the possible promotion mechanism is also raised.

2. Experimental

2.1. Chemicals

Urea (H_2NCONH_3) and bismuth nitrate pentahydrate ($Bi(NO_3)_3 \cdot 5H_2O$) were purchased from Sinopharm Chemical Reagent Corp, P. R. China. All of these purchased reagents are of analytical grade and used directly.

2.2. Synthesis

Pure g-C_3N_4 was obtained by heating urea in air at 550 °C for 2 h. The Bi_2O_3/g-C_3N_4 composites with different Bi_2O_3 mass ratio (0, 20, 40, 60 and 80 wt%) were gained through the following procedure: g-C_3N_4 (0.5 g) was dissolved in 60 mL of ethylene glycol and sonicated for 30 min to yield the g-C_3N_4 sheet. Subsequently, a certain amount (0.104, 0.208, 0.312, 0.416 g) of Bi $(NO_3)_3 \cdot 5H_2O$ and urea (1 g) were added in the solution and stirred for 1 h. The solution was then transfer to Teflon-lined autoclave (100 mL) and hydrothermally treated at 180 °C for 12 h. The obtained product was rinsed several times with deionized water and dried overnight at 80 °C. The hydrothermal product was then calcined in air at 380 °C for 2 h to get the final product. Pure Bi_2O_3 was obtained by the same procedure without the adjunction of g-C_3N_4.

2.3. Characterization

The crystal phase of catalyst was determined by X-ray diffraction (XRD, Bruker D8, Cu Kα radiation), and the morphology of the synthesized samples were investigated by scanning electron microscope (SEM, Phillips XL-30 FEG/NEW) and transmission electron microscope (TEM, Phillips Model CM200). The chemical elements of the compositions were analyzed by X-ray photoelectron spectroscopy (XPS, ESCALAB 250xi, USA) and Al Kα radiation sources. The Brunauer–Emmett–Teller (BET, Quantachrome Autosorb-iQ-AG instrument) pore structure and surface area were measured by N_2 adsorption–desorption at −196 °C. UV-vis diffuse reflectance spectrum was analyzed in the range of 250–800 nm on a spectrophotometer (SHIMADZU UV-3600, Japan) using $BaSO_4$ as the reflectance standard material. Photoluminescence (PL) was measured by a fluorescence spectrophotometer (Hitachi F-4600, 325 nm excitation wavelength).

2.4. Photoelectrochemical

Photoelectrochemical included electrochemical impedance spectroscopy (EIS) and transient photocurrent responses analysis were carried out on an electrochemical instrument (CHI 660E). A standard three-electrode system was immersed in a Na_2SO_4 electrolyte solution (0.5 M). The Pt and Ag/AgCl electrodes were used as counter and reference electrodes, respectively. FTO conductive glass covered by the synthesized sample was used as working electrode, and it was gained by the following method: mixture solution was consisted of Nafion (20

μL, 5%) and ethanol (1 mL). After that, 10 mg of the synthesized sample was dropped into the mixed solution and ultrasonically dispersed (2 h), then drop the slurry (0.1 mL) on 1 × 1 cm FTO glass. Therefore, the sample was well attached to the surface of the glass piece after evaporation of the ethanol. In addition, photocurrent and EIS measurements were performed under the illumination of the simulated solar light.

2.5. Photoactivity

The CO_2 photoreduction experiment was performed with a reactor (500 mL) in a gas-enclosed circulation system. During the reaction, a Xenon lamp (300 W) was used as the light source. The experimental procedure was designed as follows: 50 mg sample was dispersed in 100 mL deionized water, then magnetic stirring was performed at an appropriate rotation speed. The reactor was vacuum treated and 100 kPa of high purity CO_2 was passed into the reactor under the throttling of airflow. Then this pressure was kept for 30 min to obtain the balance of adsorption–desorption. Throughout the experiment, the temperature was maintained at 25 °C. The gas (0.15 mL) in reactor was obtained and analyzed by a gas chromatography (GC-2010 Plus, SHIMADZU, Japan) in the course of the reaction.

3. Results and discussion

3.1. SEM, XRD and TEM

The SEM patterns of g-C_3N_4, Bi_2O_3 and Bi_2O_3/g-C_3N_4 composites are exhibited in Fig. 1. Clearly, the g-C_3N_4 exhibits a curled layered structure (Fig. 1a), and the Bi_2O_3 shows a distinct rod-like structure (Fig. 1b). Fig. 1c shows the SEM image of 40 wt% Bi_2O_3/g-C_3N_4 sample and its corresponding elemental mapping images. It could be observed from Fig. 1c that 40 wt% Bi_2O_3/g-C_3N_4 composite perfectly retains the form of Bi_2O_3 and g-C_3N_4, showing a curled sheet structure. In addition, the mapping images of 40 wt% Bi_2O_3/g-C_3N_4 composite in Fig. 1c also reveals the coexistence of C, N, O and Bi elements.

The XRD patterns of all composites are displayed in Fig. 2. In the pattern of g-C_3N_4, the diffraction peak observed at 27.3° could be attributed to the (002) plane of g-C_3N_4 (JCPDS 87-1526). The peak at 12.7° is the (100) plane of g-C_3N_4, corresponding to the in-plane structure packing motif of tri-s-triazine units.[43] The synthesized Bi_2O_3 represents six major peaks at $2\theta = 27.8°$, 31.7°, 32.6°, 46.2°, 55.4° and 74.4°, corresponding to the (201), (002), (220), (222), (421) and (423) planes respectively, which is in consistent with the β-Bi_2O_3 (JCPDS 65-1209). As the content of Bi_2O_3 in Bi_2O_3/g-C_3N_4 samples increase, the intensity of g-C_3N_4 peak becomes weaker. As a contrast, the peak intensity of Bi_2O_3 becomes stronger, especially for the diffraction peak at 27.8°, revealing the increased crystallinity of Bi_2O_3.

The TEM images of samples are demonstrated in Fig. 3. Fig. 3a and b reveal the microscale morphology of g-C_3N_4 and Bi_2O_3, which are characterized by a curled edge and a rod-like structure respectively, as also revealed by the SEM patterns. The TEM pattern of 40 wt% Bi_2O_3/g-C_3N_4 composite shows that Bi_2O_3 and g-C_3N_4 are combined together uniformly (Fig. 3c). In addition, the 0.318 nm interplanar spacing corresponding to
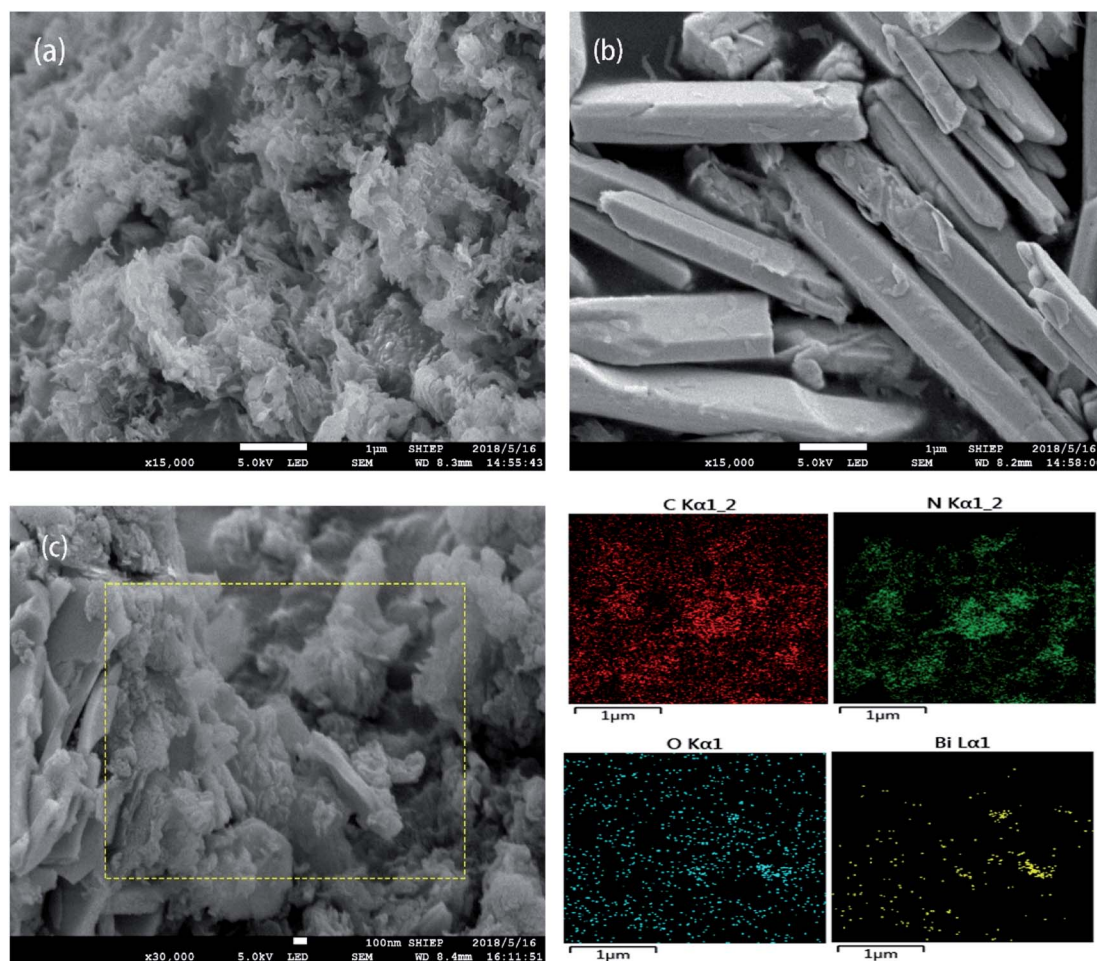
Fig. 1   SEM of g-C$_3$N$_4$ (a) and Bi$_2$O$_3$ (b); SEM and elemental mapping of C, N, O and Bi in 40 wt% Bi$_2$O$_3$/g-C$_3$N$_4$ composite (c).
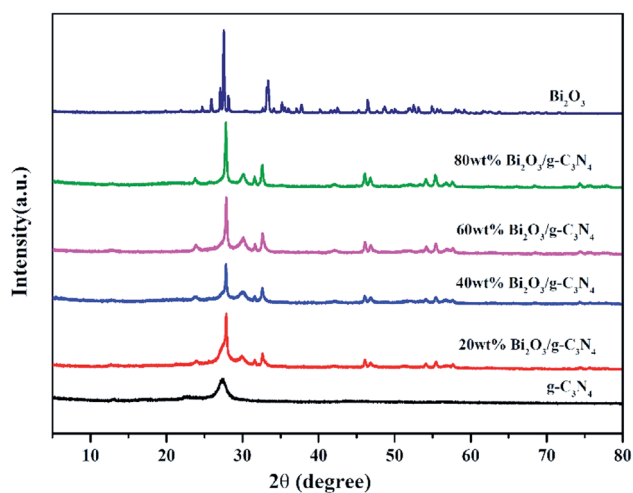
Fig. 2   XRD of g-C$_3$N$_4$, Bi$_2$O$_3$ and Bi$_2$O$_3$/g-C$_3$N$_4$ composites.

Fig. 3   TEM image of g-C$_3$N$_4$ (a), Bi$_2$O$_3$ (b) and 40 wt% Bi$_2$O$_3$/g-C$_3$N$_4$ (c); HRTEM of 40 wt% Bi$_2$O$_3$/g-C$_3$N$_4$ (d).

the (201) crystal plane of the cubic Bi$_2$O$_3$ is visible in the high resolution TEM image (Fig. 3d).[44] The results show that g-C$_3$N$_4$ and the rod-like Bi$_2$O$_3$ have deeply combined together in 40 wt% Bi$_2$O$_3$/g-C$_3$N$_4$ composite.
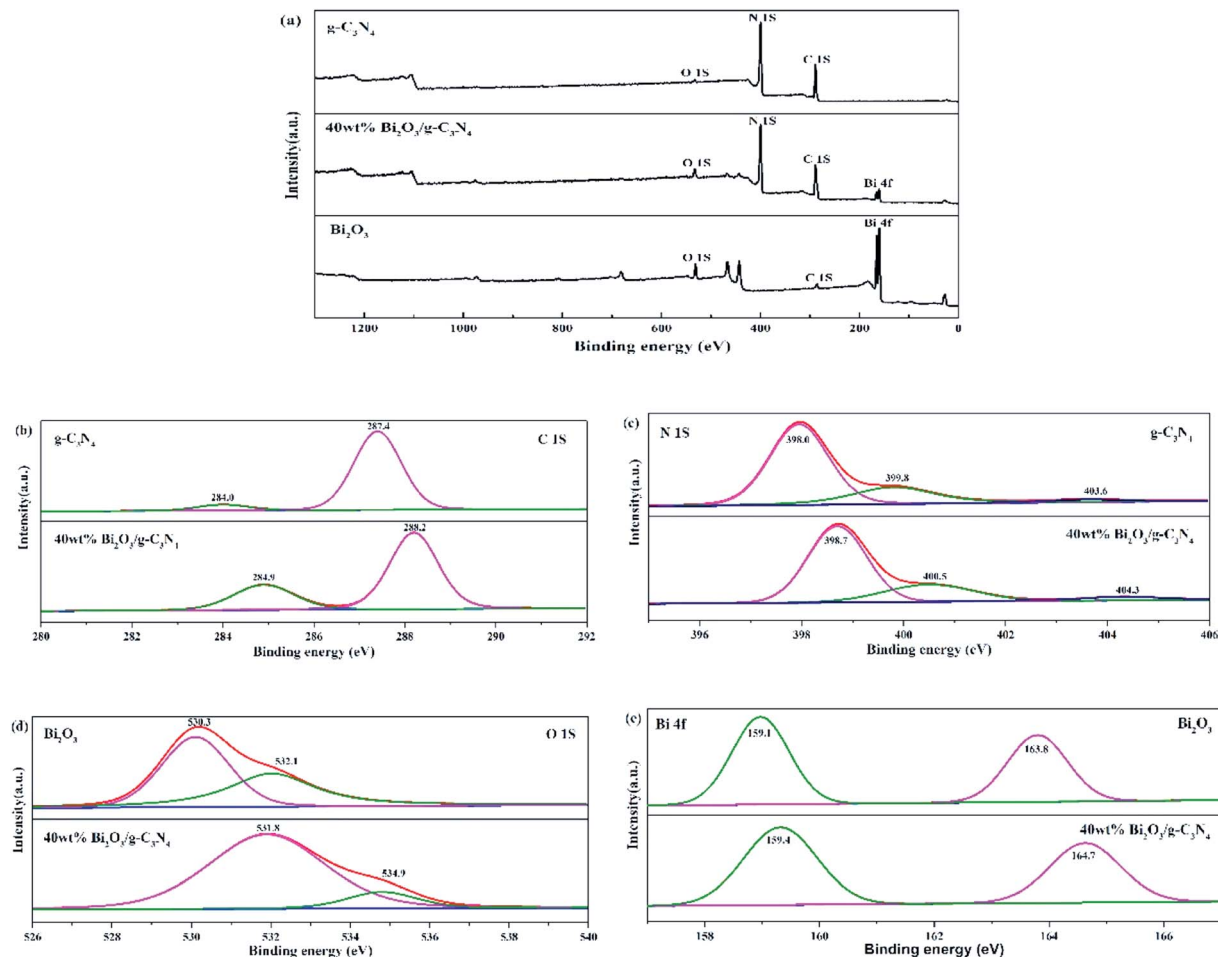
Fig. 4 XPS of g-C$_3$N$_4$, Bi$_2$O$_3$ and 40 wt% Bi$_2$O$_3$/g-C$_3$N$_4$ (a); high-resolution C 1s (b) and N 1s (c) of g-C$_3$N$_4$ and 40 wt% Bi$_2$O$_3$/g-C$_3$N$_4$; high-resolution O 1s (d) and Bi 2p (e) of Bi$_2$O$_3$ and 40 wt% Bi$_2$O$_3$/g-C$_3$N$_4$.
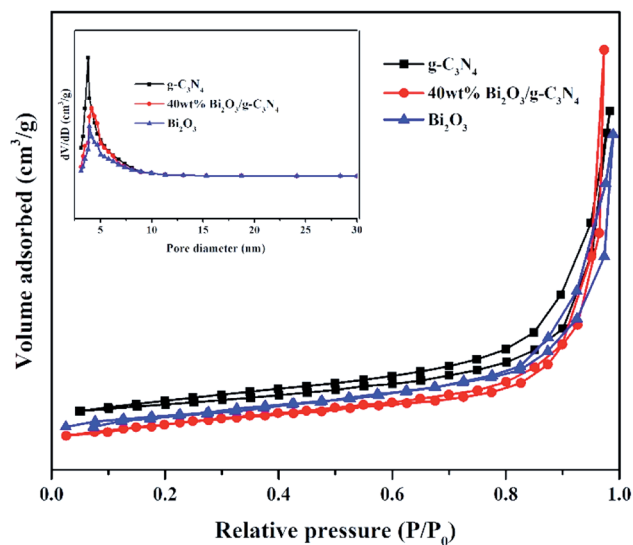

Fig. 5 N$_2$ adsorption–desorption isotherms and pore size distribution curves (inset) of g-C$_3$N$_4$, Bi$_2$O$_3$ and 40 wt% Bi$_2$O$_3$/g-C$_3$N$_4$ composite.

Table 1 Textural properties of g-C$_3$N$_4$, Bi$_2$O$_3$ and Bi$_2$O$_3$/g-C$_3$N$_4$ composites

Samples	S_{BET} (m^2 g^{-1})	Pore size (nm)
g-C$_3$N$_4$	66.7	3.839
20 wt% Bi$_2$O$_3$/g-C$_3$N$_4$	109.2	3.834
40 wt% Bi$_2$O$_3$/g-C$_3$N$_4$	136.1	3.821
60 wt% Bi$_2$O$_3$/g-C$_3$N$_4$	98.3	3.849
80 wt% Bi$_2$O$_3$/g-C$_3$N$_4$	78.2	3.815
Bi$_2$O$_3$	53.2	3.856

3.2. XPS, BET and UV

The compositions of chemical elements on g-C$_3$N$_4$, Bi$_2$O$_3$ and 40 wt% Bi$_2$O$_3$/g-C$_3$N$_4$ were analyzed by XPS. As the XPS spectra show (Fig. 4a), C 1s and N 1s signals are available in g-C$_3$N$_4$, Bi$_2$O$_3$ and 40 wt% Bi$_2$O$_3$/g-C$_3$N$_4$, while Bi 4f and O 1s peaks are detected in Bi$_2$O$_3$ and 40 wt% Bi$_2$O$_3$/g-C$_3$N$_4$ respectively, which means that Bi$_2$O$_3$ is successfully doped into g-C$_3$N$_4$. Carbon contained in Bi$_2$O$_3$ sample might be caused by extraneous carbon. The corresponding detailed spectra of C 1s, N 1s, O 1s
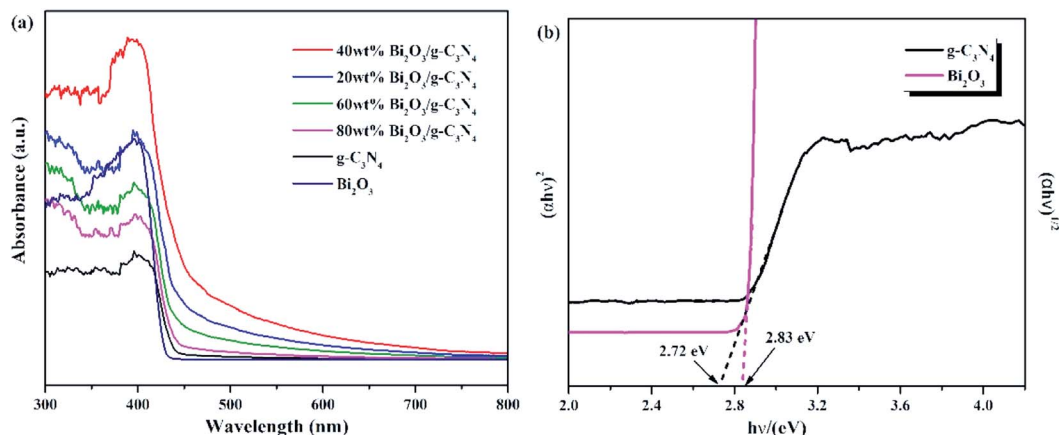
Fig. 6 (a) UV-vis DRS for g-C_3N_4, Bi_2O_3 and Bi_2O_3/g-C_3N_4 composites. (b) $(\alpha h\nu)^{1/2}$ and $(\alpha h\nu)^2$ *versus* energy ($h\nu$) for the band gap energies of g-C_3N_4 and Bi_2O_3, respectively.

and Bi 4f are also exhibited in Fig. 4. In the C 1s spectrum of g-C_3N_4, two sub-bands centered at 287.4 and 284.0 eV could be observed (Fig. 4b), corresponding to the N–C=N group and the C–C bond, respectively.[45] Fig. 4c exhibits the N 1s spectra of g-C_3N_4 and 40 wt% Bi_2O_3/g-C_3N_4. The dominant peak at 398.0 eV could be considered as the carbon-bonded sp^2-hybrid aromatic N (C=N–C),[46] while the other two peaks located at 399.8 eV and 403.6 eV could be attributed to the tertiary nitrogen N–$(C)_3$ groups and π excitations.[47] The high-resolution O 1s spectrum of Bi_2O_3 is shown in Fig. 4d, in which the protruding peaks at 530.3 eV and 532.1 eV are derived from the Bi–O bond. Two peaks are observed in high-resolution Bi 4f spectrum of Bi_2O_3 (Fig. 4e): the peak of Bi 4f at 159.1 eV and 163.8 eV reveal the presence of Bi^{3+} in Bi_2O_3.[48,49] The band energy shift of most peaks could be found in the spectrum of the 40 wt% Bi_2O_3/g-C_3N_4. The shift should be originated from the different electron concentrations,[50] which are corresponding to the SEM, XRD and TEM results mentioned above.

Nitrogen adsorption–desorption measurements were performed at −196 °C to analyze the textural features of the Bi_2O_3, g-C_3N_4 and 40 wt% Bi_2O_3/g-C_3N_4 composite. All samples show a type IV isotherm with a hysteresis loop (Fig. 5), revealing the presence of mesoporous structure into the composite. The specific surface area and average pore size of photocatalysts are listed in Table 1. Obviously, 40 wt% Bi_2O_3/g-C_3N_4 composite possesses the largest specific surface area (136.1 m^2 g^{-1}), while that for g-C_3N_4 and Bi_2O_3 are 66.7 m^2 g^{-1} and 53.2 m^2 g^{-1} respectively. Correspondingly, more active sites are available on 40 wt% Bi_2O_3/g-C_3N_4 composite. The BJH pore size distribution of g-C_3N_4, Bi_2O_3 and 40 wt% Bi_2O_3/g-C_3N_4 is shown in the inset of Fig. 5. Obviously, all the three samples exhibit a fairly narrow and limited pore size distribution between 3.6–4.1 nm.

The optical properties of Bi_2O_3, g-C_3N_4, and Bi_2O_3/g-C_3N_4 composites were tested by UV-vis measurement, and the relevant data were converted from the Kubelka–Munk equation. The 450 nm absorption edge of g-C_3N_4 could be observed in Fig. 6a, while the Bi_2O_3 shows a similar absorption properties. It can be found that Bi_2O_3/g-C_3N_4 samples could obtain more photons during the reaction according to the vertical coordinates, which is good to the photoreduction of CO_2. The band gap energy of Bi_2O_3 and g-C_3N_4 could be figured out by the formula: $\alpha h\nu = A (h\nu - E_g)^{n/2}$, where α, h, ν, A and E_g are the
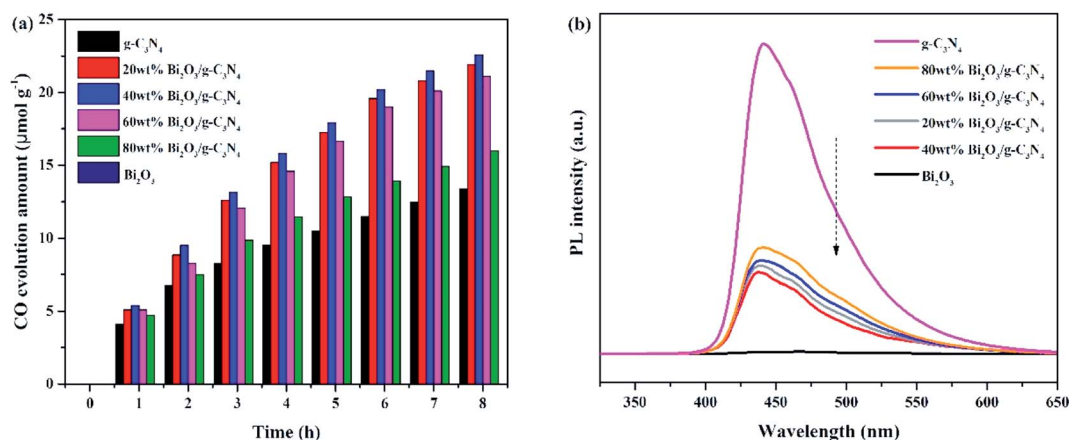

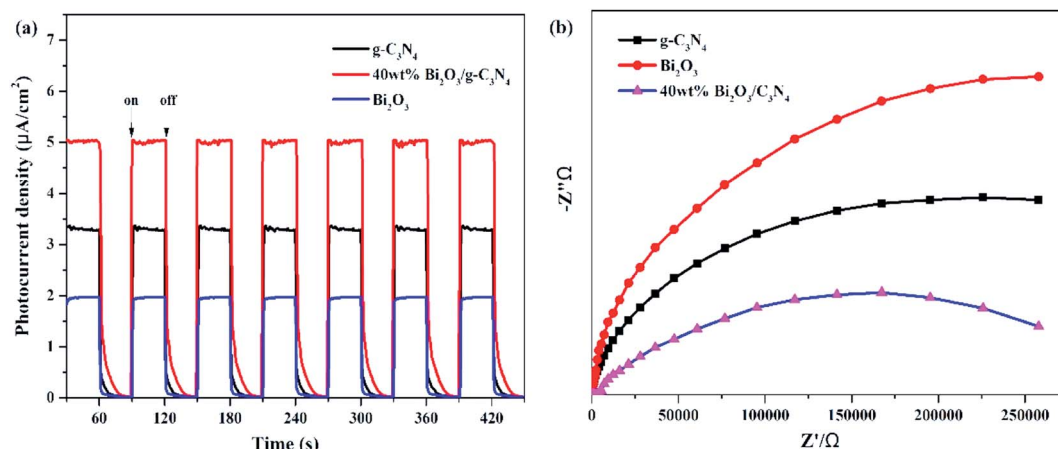**Fig. 7** (a) Yield of CO and (b) PL spectra of all samples.

Fig. 8 (a) Transient photocurrent density and (b) electrochemical impedance spectra of Bi_2O_3, g-C_3N_4 and 40 wt% Bi_2O_3/g-C_3N_4 composite.

absorption coefficient, Planck constant, light frequency, band gap energy and constant related to the catalyst. Among them, n relies on optical transition type of the semiconductor ($n = 4$ for indirect transition and $n = 1$ for direct transition). For Bi_2O_3 and g-C_3N_4, the values of n are 1 and 4, respectively.[51–53] According to Fig. 6b, the E_g values of Bi_2O_3 and g-C_3N_4 are counted to be 2.83 and 2.72 eV respectively.

3.3. Photocatalytic activity, PL and photoelectrochemical

The photocatalytic activities of all samples are tested and CO was found as the main product. In addition, the control experiments were also conducted. No hydrocarbon products are tested without simulated solar light or sample, revealing that the conditions mentioned above are essential for the CO_2 photocatalytic reduction. Fig. 7a demonstrated the amount of CO production over the photocatalysts during the light irradiation. It could be clearly seen that the pure Bi_2O_3 sample has not produced any CO, which means that pure Bi_2O_3 cannot reduce CO_2 to CO under photocatalytic conditions, due to the fact that the CB edge of Bi_2O_3 is lower than the reduction potential of CO_2/CO (-0.52 V $vs.$ NHE).[54] The yield of g-C_3N_4 is also not high, indicating that the photocatalytic performance of pure catalyst is not very well, which can be ascribed to the fast recombination

Table 2 The production rate of redox products for g-C_3N_4 and 40 wt% Bi_2O_3/g-C_3N_4

| Sample | Reduction products (μmol g^{-1} h^{-1}) | | | Oxidation products (μmol g^{-1} h^{-1}) | Ratio |
	CO	CH$_4$	H$_2$	O$_2$	e$^-$: h$^+$
g-C_3N_4	1.68	0.38	1.11	2.42	0.89 : 1
40 wt% Bi_2O_3/g-C_3N_4	2.81	1.34	1.38	6.95	0.88 : 1

rate of electron–hole pairs in reaction. A great enhancement of CO yield is detected in terms of the Bi_2O_3/g-C_3N_4 composites. Moreover, the photocatalytic activity enhances as the increasing Bi_2O_3 content in the composites, which is owing to the increased quantity of the heterojunctions. During the reaction, the highest CO yield (22.5 μmol g^{-1}) is achieved on 40 wt% Bi_2O_3/g-C_3N_4, which is about 1.8 times the CO yield of g-C_3N_4. However, the photocatalytic performance would decline along with the excessive addition of Bi_2O_3, which might be aroused by the reduce of the specific surface area, and the excessive Bi_2O_3 might act as the recombination core of electron–hole pairs

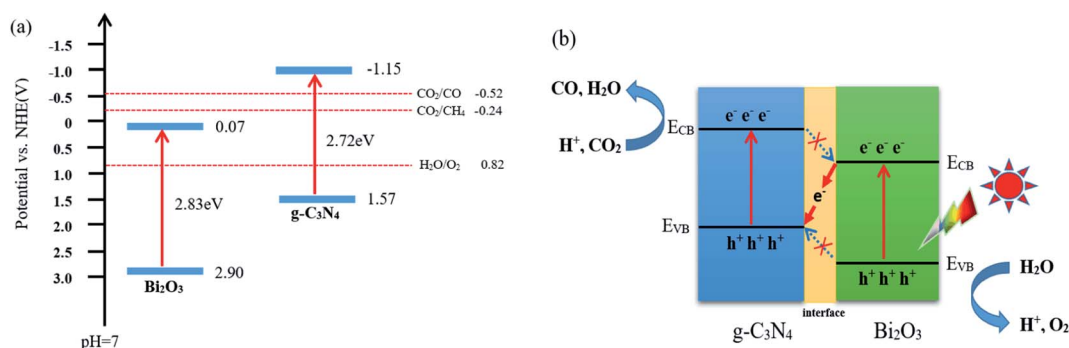Fig. 9 (a) Band gap energy and band positions of Bi_2O_3 and g-C_3N_4 together with CO_2/CO, CO_2/CH$_4$ and H_2O/O_2 redox potentials at pH = 7 and (b) Z-type mechanism of CO_2 photoreduction route on Bi_2O_3/g-C_3N_4 composite.

during the reaction.[55,56] The photocatalytic stability of all composites and g-C₃N₄ are shown in the Fig. S1,† the yield of CO keeps stable during three experimental runs, revealing that the performance of all composites and g-C₃N₄ are stable during the reaction. To further probe the truth, the separation efficiency was characterized by PL. As shown in Fig. 7b, the emission peak of Bi_2O_3 is almost invisible in the 450–500 nm range, which may be due to a trace of surface defects or surface oxygen vacancies of Bi_2O_3. Compared with Bi_2O_3, a strong peak concentrated at 450 nm could be noticed in the g-C₃N₄ spectrum, which reflects the fast recombination rate of electrons–hole pairs.[57] Different from g-C₃N₄, the Bi_2O_3/g-C₃N₄ composites exhibit a moderate peak intensity in the pattern, suggesting that heterojunctions are built among Bi_2O_3 and g-C₃N₄, so the holes and electrons are effectively separated. Therefore, the recombination rate is greatly reduced, which is good to enhance the activity of CO_2 photoreduction. In addition, the 40 wt% Bi_2O_3/g-C₃N₄ has the lowest peak intensity among all the synthesized Bi_2O_3/g-C₃N₄ samples.

In addition to PL measurements, photo-electrochemical measurements are used to further analyze the properties of photoelectrons in Bi_2O_3, g-C₃N₄ and 40 wt% Bi_2O_3/g-C₃N₄. Fig. 8a shows the photocurrent response of the samples under visible light absorption. Transient photocurrent measurements could show more evidence for the rapid electron transfer efficiency in the photocatalyst. In the light-on and light-off tests, all the photocatalysts show rapid and intense photocurrent response, indicating that the photocatalytic activity is relatively stable. Both Bi_2O_3 and g-C₃N₄ exhibit a rapidly increasing current when light is on and an abruptly decreasing signal when the light is off. This transient response behavior might be resulted from the capture and release of electrons caused by surface defects.[58] In addition, the photocurrent intensity of 40 wt% Bi_2O_3/g-C₃N₄ heterostructured composite is 2.5 and 1.5 times the intensity of Bi_2O_3 and g-C₃N₄, respectively, indicating that 40 wt% Bi_2O_3/g-C₃N₄ has higher charge separation efficiency and better photocatalytic properties than pure catalysts. To confirm this inference, the EIS experiment was also performed. The semicircular Nynquist plots of the samples are presented in Fig. 8b. Obviously, a smaller semicircle diameter could be detected on the plot of 40 wt% Bi_2O_3/g-C₃N₄ than that of pure Bi_2O_3 and pure g-C₃N₄, indicating that the electron transfer rate is faster in 40 wt% Bi_2O_3/g-C₃N₄,[59] which is corresponding to the previous photocatalytic activity results.

3.4. Mechanism

According to the characterization and CO_2 photocatalytic reduction test results of the prepared samples, the reaction mechanism of CO_2 reduction over Bi_2O_3/g-C₃N₄ composites were proposed. As shown in Fig. 9a, the valence band (VB) and conduction band (CB) of a semiconductor could be determined using the following equation:[60] $E_{CB}^0 = \chi - E^C - 1/2E_g$. Where χ is the absolute electronegativity of the semiconductor (χ for Bi_2O_3 is 5.986 eV), E^C is the energy of free electrons in the hydrogen size (4.5 eV) and E_g is the band gap of the semiconductor.[61,62] Combined with the results in Fig. 6b, the conduction band (CB)

and valence band (VB) values for the pure Bi_2O_3 are 0.07 eV and 2.90 eV, respectively. For g-C₃N₄, the VB is −1.57 eV, and the CB is 1.15 eV.[63,64] The charge transfer in the interface can follow a double-transfer mode or a Z-scheme transfer mechanism. Double-transfer means that the CO_2 reduction reaction would happen on the CB of Bi_2O_3, and the H_2O oxidation reaction would occur on the VB of g-C₃N₄. In fact, the CB of Bi_2O_3 is lower than the reduction potential level of CO_2/CO (−0.52 V vs. NHE), thus the reduction of CO_2 would not proceed and CO would not be generated, which means that double-transfer mechanism is not suitable here to explain. Z-scheme transfer mechanism is different from the double-transfer mechanism, as shown in Fig. 9b, the photo-induced electrons on the surface of Bi_2O_3 can easily be transferred to g-C₃N₄ through the interface, the holes on VB of Bi_2O_3 are captured by H_2O molecules to produce O_2 and protons. At the same time, the CO_2 molecules react with the electrons on the CB of g-C₃N₄ to generate CO and H_2O with the participation of protons. Moreover, the formation of other products including CH_4, H_2, and O_2 were also observed in the experimental process, and the charge balance table is shown in Table 2. The enhanced activity of 40 wt% Bi_2O_3/g-C₃N₄ in CO_2 reduction is mainly due to the Z-scheme heterostructure, which effectively delays the rapid recombination of the electron–hole pairs in Bi_2O_3 and g-C₃N₄, therefore improving the photocatalytic activity.

4. Conclusions

In general, Bi_2O_3/g-C₃N₄ nanoscale composites with heterojunction was successfully synthesized by the combination of high temperature calcination and hydrothermal method. The 40 wt% Bi_2O_3/g-C₃N₄ composite has the highest CO yield in the CO_2 photocatalytic reduction, which is 1.8 times the yield of that g-C₃N₄. This obvious improvement in photoactivity is mainly due to the effective separation of electron–hole pairs and successive charge transfer through the interface. Moreover, the enhancement of specific surface area and visible light response also upgrade the photocatalytic performance of Bi_2O_3/g-C₃N₄ composite. This study gives some valuable opinion for the research of g-C₃N₄-related photocatalysts.

Conflicts of interest

There are no conflicts to declare.

Acknowledgements

References

1 S. Zhou, Y. Liu, J. M. Li, Y. J. Wang, G. Y. Jiang, Z. Zhao, D. X. Wang, A. J. Duan, J. Liu and Y. C. Wei, *Appl. Catal., B*, 2014, **158–159**, 20–29.

2 G. G. Zhang, G. S. Li, T. Heil, S. Zafeiratos, F. L. Lai, A. Savateev, M. Antonietti and X. C. Wang, *Angew. Chem., Int. Ed.*, 2019, **58**, 3433–3437.

3 H. B. Yu, B. B. Huang, H. Wang, X. Z. Yuan, L. B. Jiang, Z. B. Wu, J. Zhang and G. M. Zeng, *J. Colloid Interface Sci.*, 2018, **522**, 82–94.

4 H. B. Yu, L. B. Jiang, H. Wang, B. B. Huang, X. Z. Yuan, J. H. Huang, J. Zhang and G. M. Zeng, *Small*, 2019, **15**, 1901008.

5 Y. Yang, Z. T. Zeng, G. M. Zeng, D. L. Huang, R. Xiao, C. Zhang, C. Y. Zhou, W. P. Xiong, W. J. Wang, M. Cheng, W. J. Xue, H. Guo, X. Tang and D. H. He, *Appl. Catal., B*, 2019, **258**, 117956.

6 H. Yi, M. Jiang, D. L. Huang, G. M. Zeng, C. Lai, L. Qin, C. Y. Zhou, B. S. Li, X. G. Liu, M. Cheng, W. J. Xue, P. Xu and C. Zhang, *J. Taiwan Inst. Chem. Eng.*, 2018, **93**, 184–192.

7 J. Xu, K. K. Wang, T. Liu, Y. Peng and B. G. Xu, *CrystEngComm*, 2017, **19**, 5001–5007.

8 S. M. Lopez, V. Vaiano, M. C. Hidalgo, J. A. Navio and D. Sannino, *Photochem. Photobiol. Sci.*, 2015, **14**, 678–685.

9 J. J. Wang, L. Tang, G. M. Zeng, Y. C. Deng, Y. N. Liu, L. L. Wang, Y. Y. Zhou, Z. Guo, J. J. Wang and C. Zhang, *Appl. Catal., B*, 2017, **209**, 285–294.

10 H. F. Cheng, B. B. Huang, Y. Y. Liu, Z. Y. Wang, X. Y. Qin, X. Y. Zhang and Y. Dai, *Chem. Commun.*, 2012, **48**, 9729–9731.

11 M. Sierra, E. Borges, P. Esparza, J. M. Ramos, J. M. Gil and P. M. Ramos, *Sci. Technol. Adv. Mater.*, 2016, **17**, 659–668.

12 C. Y. Liu, H. W. Huang, X. Du, T. R. Zhang, N. Tian, Y. X. Guo and Y. H. Zhang, *J. Phys. Chem. C*, 2015, **119**, 17156–17165.

13 H. H. Yang, Y. Bai, T. Chen, X. Shi and Y. C. Zhu, *Phys. E*, 2016, **78**, 100–104.

14 X. Y. Liu, R. T. Guo, H. Qin, Z. Y. Wang, X. Shi, W. G. Pan, J. Y. Tang, P. Y. Jia, Y. F. Miao and J. W. Gu, *Colloids Surf., A*, 2019, **580**, 123782.

15 R. T. Guo, X. Y. Liu, H. Qin, Z. Y. Wang, X. Shi, W. G. Pan, Z. G. Fu, J. Y. Tang, P. Y. Jia, Y. F. Miao and J. W. Gu, *Appl. Surf. Sci.*, 2020, **500**, 144069.

16 J. C. Wang, H. C. Yao, Z. Y. Fan, L. Zhang, J. S. Wang, S. Y. Zang and Z. J. Li, *ACS Appl. Mater. Interfaces*, 2016, **8**, 3765–3775.

17 N. Tian, H. W. Huang, Y. X. Guo, Y. He and Y. H. Zhang, *Appl. Surf. Sci.*, 2014, **322**, 249–254.

18 G. P. Gao, Y. Jiao, E. R. Waclawik and A. J. Du, *J. Am. Chem. Soc.*, 2016, **138**, 6292–6297.

19 X. F. Chen, J. S. Zhang, X. Z. Fu, M. Antonietti and X. C. Wang, *J. Am. Chem. Soc.*, 2009, **131**, 11658–11659.

20 K. Wang, Q. Li, B. S. Liu, B. Cheng, W. K. Ho and J. G. Yu, *Appl. Catal., B*, 2015, **176–177**, 44–52.

21 D. D. Zheng, C. J. Huang and X. C. Wang, *Nanoscale*, 2015, **7**, 465–470.

22 X. J. Bai, J. Li, C. B. Cao and S. Hussain, *Mater. Lett.*, 2011, **65**, 1101–1104.

23 X. S. Zhou, B. Jin, L. D. Li, F. Peng, H. J. Wang, H. Yu and Y. P. Fang, *J. Mater. Chem.*, 2012, **22**, 17900–17905.

24 J. L. Zhao, Z. Y. Ji, X. P. Shen, H. Zhou and L. B. Ma, *Ceram. Int.*, 2015, **41**, 5600–5606.

25 M. L. Li, L. X. Zhang, X. Q. Fan, M. Y. Wu, M. Wang, R. L. Cheng, L. L. Zhang, H. L. Yao and J. L. Shi, *Appl. Catal., B*, 2017, **201**, 629–635.

26 M. L. Li, L. X. Zhang, M. Y. Wu, Y. Y. Du, X. Q. Fan, M. Wang, L. L. Zhang, Q. L. Kong and J. L. Shi, *Nano Energy*, 2016, **19**, 145–155.

27 M. Wang, M. Shen, L. X. Zhang, J. J. Tian, X. X. Jin, Y. J. Zhou and J. L. Shi, *Carbon*, 2017, **120**, 23–31.

28 S. S. Yi, X. Z. Yue, D. D. Xu, Z. P. Liu, F. Zhao, D. J. Wang and Y. H. Lin, *New J. Chem.*, 2015, **39**, 2917–2924.

29 J. Lee, H. Lee and M. Kang, *Mater. Lett.*, 2016, **178**, 316–319.

30 M. Ahila, J. Dhanalakshmi, J. Selvakumari and D. Padiyan, *Mater. Res. Express*, 2016, **3**, 105025.

31 M. X. Ji, J. Di, Y. P. Ge, J. X. Xia and H. M. Li, *Appl. Surf. Sci.*, 2017, **413**, 372–380.

32 C. Chang, H. C. Yang, N. Gao and S. Y. Lu, *J. Alloys Compd.*, 2018, **738**, 138–144.

33 E. Diez, O. Monnereau, L. Tortet, G. Vacquier, P. Llewellin and F. Rouquerol, *J. Optoelectron. Adv. Mater.*, 2000, **2**, 552–556.

34 Y. P. Li, S. L. Wu, L. Y. Huang, H. Xu, R. X. Zhang, M. L. Qu, Q. Gao and H. M. Hua, *J. Phys. Chem. Solids*, 2015, **76**, 112–119.

35 W. J. Shan, Y. Hu, Z. G. Bai, M. M. Zheng and C. H. Wei, *Appl. Catal., B*, 2016, **188**, 1–12.

36 J. F. Zhang, Y. F. Hu, X. L. Jiang, S. F. Chen, S. G. Meng and X. L. Fu, *J. Hazard. Mater.*, 2014, **280**, 713–722.

37 J. J. Wang, L. Tang, G. M. Zeng, Y. N. Liu, Y. Y. Zhou, Y. C. Deng, J. J. Wang and B. Peng, *ACS Sustainable Chem. Eng.*, 2017, **5**, 1062–1072.

38 S. Y. Chai, Y. J. Kim, M. H. Jung, A. K. Chakraborty, D. W. Jung and W. I. Lee, *J. Catal.*, 2009, **262**, 144–149.

39 M. L. Guan, D. K. Ma, S. W. Hu, Y. J. Chen and S. M. Huang, *Inorg. Chem.*, 2010, **50**, 800–805.

40 J. Zhu, S. H. Wang, J. G. Wang, D. Q. Zhang and H. X. Li, *Appl. Catal., B*, 2011, **102**, 120–125.

41 L. X. Yang, S. L. Luo, Y. Li, Y. Xiao, Q. Kang and Q. Y. Cai, *Environ. Sci. Technol.*, 2010, **44**, 7641–7646.

42 C. Y. Tsai, C. W. Liu, C. H. Fan, H. C. Hsi and T. Y. Chang, *J. Phys. Chem. C*, 2017, **121**, 6050–6059.

43 X. H. Li, J. S. Chen, X. C. Wang, J. H. Sun and M. Antonietti, *J. Am. Chem. Soc.*, 2011, **133**, 8074–8077.

44 L. B. Jiang, X. Z. Yuan, G. M. Zeng, J. Liang, X. H. Chen, H. B. Yu, H. Wang, Z. B. Wu, J. Zhang and T. Xiong, *Appl. Catal., B*, 2018, **227**, 376–385.

45 Y. B. Li, H. M. Zhang, P. R. Liu, D. Wang, Y. Li and H. J. Zhao, *Small*, 2013, **9**, 3336–3344.

46 C. Z. Zhang, R. Hao, H. B. Liao and Y. L. Hou, *Nano Energy*, 2013, **2**, 88–97.

47 S. Thaweesak, M. Lyu, P. Peerakiatkhajohn, T. Butburee, B. Luo, H. J. Chen and L. Z. Wang, *Appl. Catal., B*, 2017, **202**, 184–190.

48 Z. H. Wu, J. Liu, Q. Y. Tian and W. Wu, *ACS Sustainable Chem. Eng.*, 2017, **5**, 5008–5017.

49 F. Dong, T. Xiong, R. Wang, Y. J. Sun and Y. K. Jiang, *Dalton Trans.*, 2014, **43**, 6631–6642.

50 Y. Liu, S. Yu, Z. Y. Zhao, F. Dong, X. A. Dong and Y. Zhou, *J. Phys. Chem. C*, 2017, **121**, 12168–12177.

51 J. R. Jin, Y. J. Wang and T. He, *RSC Adv.*, 2015, **5**, 100244–100250.

52 J. J. Hu, G. Q. Xu, J. W. Wang, J. Lv, X. Y. Zhang, T. Xie, Z. X. Zheng and Y. C. Wu, *Dalton Trans.*, 2015, **44**, 5386–5395.

53 J. S. Chen, S. Y. Qin, G. X. Song, T. Y. Xiang, F. Xin and X. H. Yin, *Dalton Trans.*, 2013, **42**, 15133–15138.

54 D. Wu, L. Q. Ye, H. Y. Yip and P. K. Wong, *Catal. Sci. Technol.*, 2017, **7**, 265–271.

55 F. Li, L. Zhang, X. Chen, Y. L. Liu, S. G. Xua and S. K. Cao, *Phys. Chem. Chem. Phys.*, 2017, **19**, 21862–21868.

56 C. Xue, T. X. Zhang, S. J. Ding, J. J. Wei and G. D. Yang, *ACS Appl. Mater. Interfaces*, 2017, **9**, 16091–16102.

57 T. Xiong, W. L. Cen, Y. X. Zhang and F. Dong, *ACS Catal.*, 2016, **6**, 2462–2472.

58 D. Jiang, W. Z. Wang, S. M. Sun, L. Zhang and Y. L. Zheng, *ACS Catal.*, 2015, **5**, 613–621.

59 D. Wu, L. Q. Ye, H. Y. Yip and P. K. Wong, *Catal. Sci. Technol.*, 2017, **7**, 265–271.

60 H. Xu, Y. G. Xu, H. M. Li, J. X. Xia, J. Xiong, S. Yin, C. J. Huang and H. L. Wan, *Dalton Trans.*, 2012, **41**, 3387–3394.

61 H. M. Fan, H. Y. Li, B. K. Liu, Y. C. Lu, T. F. Xie and D. J. Wang, *ACS Appl. Mater. Interfaces*, 2012, **4**, 4853–4857.

62 H. L. Li, Y. Gao, X. Y. Wu, P. H. Lee and K. Shih, *Appl. Surf. Sci.*, 2017, **402**, 198–207.

63 S. C. Yan, S. B. Lv, Z. S. Li and Z. G. Zou, *Dalton Trans.*, 2010, **39**, 1488–1491.

64 H. Qin, R. T. Guo, X. Y. Liu, W. G. Pan, Z. Y. Wang, X. Shi, J. Y. Tang and C. Y. Huang, *Dalton Trans.*, 2018, **47**, 15155–15163.